PHYSICAL REVIEW B **97**, 184102 (2018)

Computational findings of metastable ferroelectric phases of squaric acid

Shoji Ishibashi,[1] Sachio Horiuchi,[2] and Reiji Kumai[3]
[1] *Research Center for Computational Design of Advanced Functional Materials (CD-FMat), National Institute of Advanced Industrial Science and Technology (AIST), Tsukuba, Ibaraki 305-8568, Japan*
[2] *Flexible Electronics Research Center (FLEC), National Institute of Advanced Industrial Science and Technology (AIST), Tsukuba, Ibaraki 305-8565, Japan*
[3] *Condensed Matter Research Center (CMRC) and Photon Factory, Institute of Materials Structure Science, High Energy Accelerator Research Organization (KEK), Tsukuba, Ibaraki 305-0801, Japan*

(Received 8 February 2018; revised manuscript received 3 April 2018; published 14 May 2018)

Antiferroelectric-to-ferroelectric transitions in squaric acid are simulated by computationally applying a static electric field. Depending on the direction of the electric field, two different metastable ferroelectric (and piezoelectric) phases have been found. One of them corresponds to the experimentally confirmed phase, whereas the other is an optimally polarized phase. The structural details of these phases have been determined as a function of the electric field. The spontaneous polarization values of the phases are 14.5 and 20.5 $\mu\text{C/cm}^2$, respectively, and are relatively high among those of the existing organic ferroelectrics.

DOI: 10.1103/PhysRevB.97.184102

I. INTRODUCTION

Since the theoretical prediction of antiferroelectricity by Kittel [1] and its experimental discovery on $PbZrO_3$ ceramics [2,3], antiferroelectricity in inorganic materials, especially in perovskite oxides, has been extensively studied. In contrast, the research on antiferroelectricity of organic materials has been scarce [4]. Recently, antiferroelectrics have been considered to be promising materials for practical applications such as actuators, sensors, and energy-storage devices [5–7].

Among organic antiferroelectrics, squaric acid (SQA) has attracted considerable attention because of its two dimensionality owing to the pseudotetragonal symmetry of the molecular and hydrogen-bonded structures [8]. Previously, we showed direct evidence of antiferroelectricity in SQA, confirming the transition from an antiferroelectric (AFE) phase to a ferroelectric (FE) phase in the presence of a strong electric field [9]. Furthermore, we proposed two possible FE phases (FE-α and FE-β) with their molecular arrangements and space groups. Electric polarization amplitudes of the FE-α and FE-β phases were indirectly estimated to be 16.4 and 23.2 $\mu\text{C/cm}^2$, respectively, based on the experimental AFE structure [10], since detailed crystal structures of the FE phases were not determined. The point charge model could not explain these rather high polarization amplitudes and the rearrangement of the π electrons was proposed as their origin. The estimated value for the FE-α phase was in reasonable agreement with the experimental value of 10.5 $\mu\text{C/cm}^2$. However, the FE-β phase could not be practically achieved because of insufficient field strength.

In the present work, we attempt to reproduce the AFE-to-FE transition in SQA via computational simulation and to identify two metastable ferroelectric phases along with their crystal structures, spontaneous polarization values, and piezoelectric effects.

To simulate this transition under an electric field, it is necessary to reproduce the crystal structure accurately. SQA is a typical molecular solid, where the van der Waals (vdW) interaction is important for binding. Neither the local density approximation (LDA) [11,12] nor the generalized gradient approximation (GGA) [13] can describe the vdW interaction accurately. Therefore, we applied the van der Waals density functional consistent-exchange (vdW-DF-cx) [14] and revised Vydrov–Van Voorhis (rVV10) [15,16] functionals, which are recent versions of the vdW density functional theory (DFT) method originally developed by Dion *et al.* [17].

II. COMPUTATIONAL METHODS

Calculations were performed using the QMAS code [18] based on the projector augmented-wave method [19] and plane-wave basis set. The vdW-DF-cx and rVV10 functionals were implemented according to the Wu-Gygi algorithm [20,21] based on the efficient algorithm proposed by Román-Pérez and Soler [22]. The plane-wave cutoff energy was set to 20 Ha. For each calculation, $8 \times 8 \times 8$ $\boldsymbol{k}$ points in the full Brillouin zone were sampled. Structural optimization was performed by the Broyden-Fletcher-Goldfarb-Shanno (BFGS) algorithm [23] for the atomic positions and by the fast-inertial-relaxation-engine (FIRE) algorithm [24] for the lattice vectors with convergence criteria of 5×10^{-5} Ha/bohr for the maximum force and 5×10^{-7} Ha/bohr^3 for the square root of the sum of the squares of the stress components. The finite basis set correction [25] was applied for evaluating the stress components.

Calculations under a static electric field were performed according to the method proposed by Souza *et al.* [26]. The total polarization was obtained as the sum of the electronic and ionic polarizations. The electronic polarization was evaluated using the Berry phase approach [27,28], similarly to our previous studies [29,30].

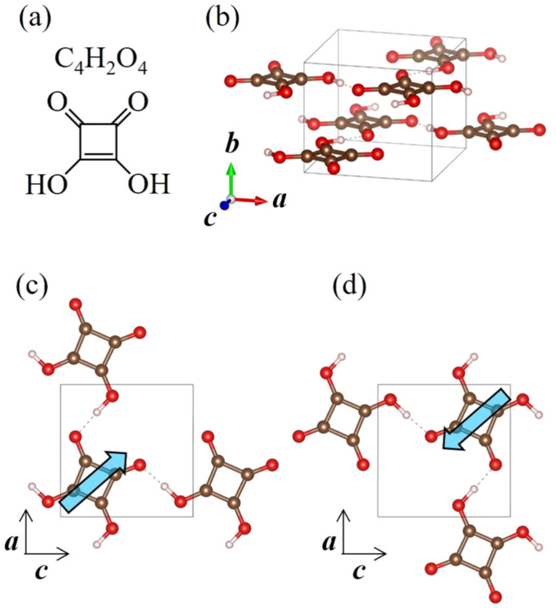

FIG. 1. Crystal structure of SQA [10]. (a) Chemical structural formula, (b) unit-cell view, (c) hydrogen-bond network at $y = 0.25$, and (d) hydrogen-bond network at $y = 0.75$. Arrows in (c) and (d) represent the sublattice polarization vector [9].

III. RESULTS AND DISCUSSION

Figure 1 shows the experimental crystal structure of SQA at room temperature [10]. There are two molecules in the unit cell. Each of them forms a planar hydrogen-bond-network sublattice at $y = 0.25$ or 0.75. The sublattice polarization vectors, which were calculated in our previous work [9], are also plotted in Fig. 1. Since there is mirror symmetry with respect to the hydrogen-bond-network plane, the polarization component along the $\boldsymbol{b}$ axis is zero. Starting from the experimental structure, the atomic positions and lattice parameters were computationally optimized using the above-mentioned vdW DFT functionals as well as LDA and GGA for comparison. The obtained lattice parameters are listed and compared with the experimental results at 15 K [31] in Table I. Since our calculations do not consider temperature effects, comparisons with the low-temperature structure are more appropriate. There are two crystallographically inequivalent hydrogen bonds. They are also listed in Table I. LDA underestimates the lattice parameters, whereas the GGA overestimates them, particularly with respect to the stacking direction of the planar molecules $\boldsymbol{b}$. A similar tendency was reported for croconic acid in a previous study [32]. These are well-known features when applied to materials exhibiting vdW interactions. The hydrogen bonds are significantly underestimated using LDA, whereas GGA gives slightly underestimated values. In general, the two vdW-DFT functionals provide better results. In particular, the values obtained by the rVV10 functional are in excellent agreement with the corresponding experimental ones. Therefore, we used the rVV10 functional for subsequent calculations.

A static electric field was applied along $\boldsymbol{x}$, z, $\boldsymbol{x}+z$, or $\boldsymbol{x}-z$, where $\boldsymbol{x} \parallel \boldsymbol{a}$ and $z \parallel \boldsymbol{c}^*$. For each case, the field was increased from zero in increments of 1 MV/cm until an expected polarization switching occurred. Then, the field was decreased to zero and proceeded in the negative direction until the polarization was inverted. In Fig. 2, in order of calculations with varying the electric field $\boldsymbol{E}$, the calculated polarization vectors are plotted in terms of the amplitude $|\boldsymbol{P}|$ and the angle $\theta_{\boldsymbol{P}}$ with respect to $\boldsymbol{x}$. The direction of $|\boldsymbol{E}|$ is also plotted as the angle $\theta_{\boldsymbol{E}}$. Several snapshots of the molecular arrangements are shown in Fig. 3 together with the sublattice polarization vectors. Since the mirror symmetry with respect to the hydrogen-bond-network plane is maintained under $\boldsymbol{E} \perp \boldsymbol{b}$, the polarization component along $\boldsymbol{b}$ is zero. For each case, the sum of the sublattice polarization vectors is nearly identical to the total polarization vector, implying that the electronic interaction between the sublattices is not strong. The deviations of $|\boldsymbol{P}|$ and $\theta_{\boldsymbol{P}}$ are, at most, 1.3% and 1.5°, respectively. It is clearly shown that the SQA crystal can be polarized along eight different directions [$\pm\boldsymbol{x}$, $\pm z$, $\pm(\boldsymbol{x}+z)$, and $\pm(\boldsymbol{x}-z)$], depending on the $\boldsymbol{E}$ direction.

For all cases, the FE phases are maintained at zero field while decreasing the electric field, whereas, in the actual experiment [9], only the AFE phase was observed at zero field. Our calculations consider zero temperature and there are no defects and no surfaces. Since there is a finite barrier between the two phases, as shown later, the system does not recover the AFE phase even at zero field. It should be mentioned that the switching field for each is much higher than that observed in the experimental results [9]. In addition, the assumption of simultaneous motion in the periodic arrangement of unit cells in the present calculations is thought to be another reason. Such an overestimation of the switching field in the theoretical calculation was also reported for $AgNbO_3$ [33]. For the $\boldsymbol{E} \parallel \boldsymbol{x}$ and $\boldsymbol{E} \parallel z$ cases, the AFE-to-FE transition occurs at a lower electric field compared with the $\boldsymbol{E} \parallel \boldsymbol{x}+z$ and $\boldsymbol{E} \parallel \boldsymbol{x}-z$ cases. A similar tendency was observed in our previous experiments [9], although the electric-field strength was much lower than that in the present computational study, as mentioned above. For $\boldsymbol{E} \parallel \boldsymbol{x}+z$, the AFE-to-FE transition occurs in two steps. Similarly, for $\boldsymbol{E} \parallel \boldsymbol{x}-z$ in the negative direction, the polarization inversion occurs in two steps.

TABLE I. Lattice parameters and hydrogen-bond lengths of SQA obtained using various exchange-correlation functionals. The values in the parentheses represent deviations from the experimental values at 15 K (in percentage).

	a (Å)	b (Å)	c (Å)	β (°)	$d_{O\cdots O}$ (Å)	
Expt. (15 K)[1]	6.118	5.140	6.130	89.74	2.544	2.552
LDA	6.019 (−1.6)	4.919 (−4.3)	6.019 (−1.8)	90.00	2.413	2.413
GGA	6.192 (+1.2)	6.126 (+19.2)	6.203 (+1.2)	89.89	2.505	2.511
vdW-DF-cx	6.096 (−0.36)	5.381 (+4.7)	6.103 (−0.44)	89.97	2.484	2.486
rVV10	6.127 (+0.15)	5.143 (+0.06)	6.142 (+0.20)	89.92	2.537	2.542

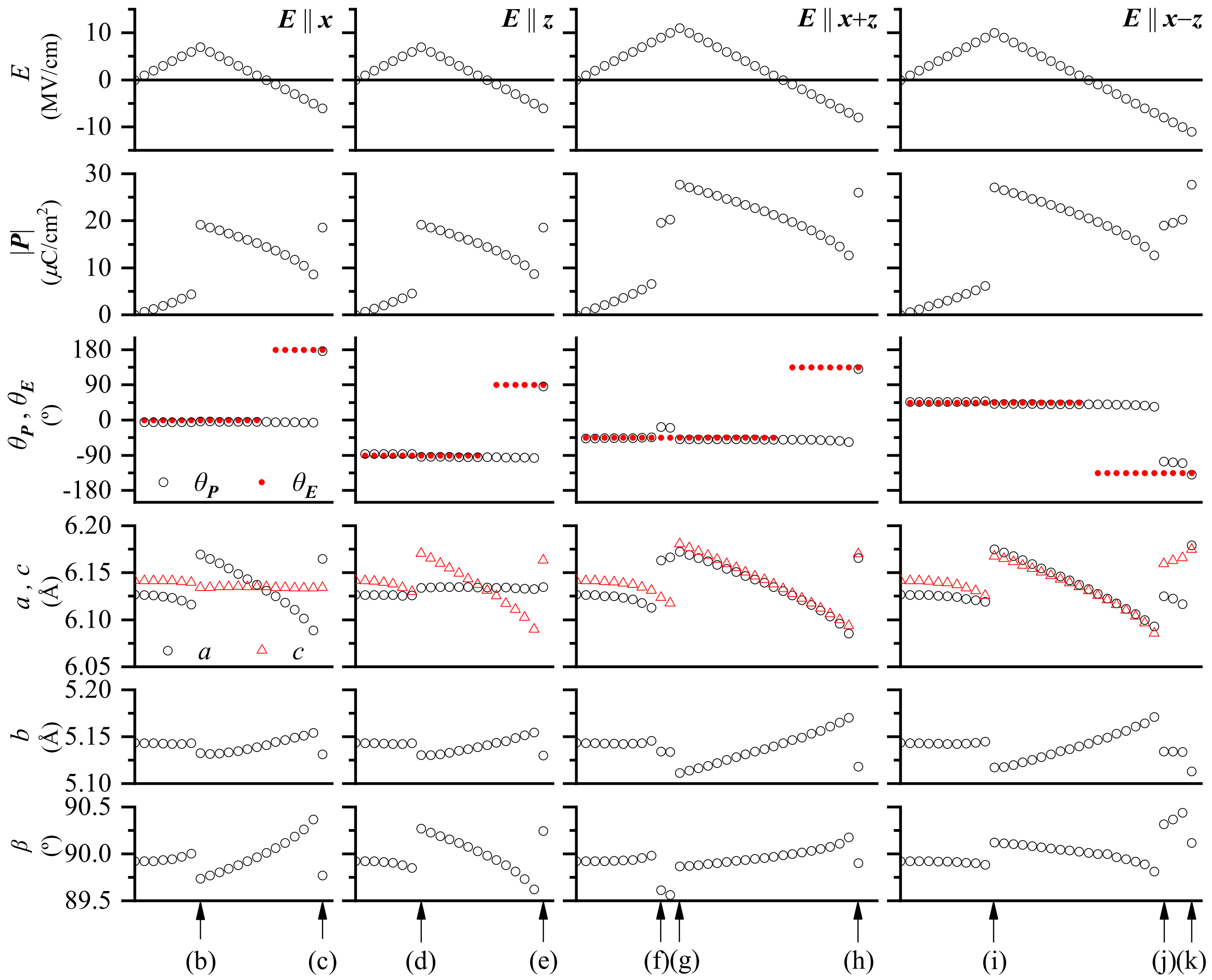

FIG. 2. Variations of polarization vectors and lattice parameters of SQA under electric field ($\boldsymbol{E} \parallel \boldsymbol{x}$, $\boldsymbol{z}$, $\boldsymbol{x}+\boldsymbol{z}$, and $\boldsymbol{x}-\boldsymbol{z}$). In each panel, values are plotted from left to right in order of calculations with varying $\boldsymbol{E}$. $\theta_{\boldsymbol{P}}$ ($\theta_{\boldsymbol{E}}$) is the angle between $\boldsymbol{P}$ ($\boldsymbol{E}$) and $\boldsymbol{x}$. The z direction corresponds to $-90°$. Results labeled (b)–(k) correspond to panels in Fig. 3. Calculations were performed using the rVV10 functional.

However, it is thought that the transition conditions depend significantly on the increment of the electric field and the optimization schemes for the atomic positions and the lattice vectors. Here, we will not explore these problems further.

In Fig. 2, the optimized lattice parameters with varying $\boldsymbol{E}$ are also plotted. For $\boldsymbol{E} \parallel \boldsymbol{x}$ ($\boldsymbol{E} \parallel \boldsymbol{z}$), after the switching to the FE phase occurs, the lattice parameter a (c) shows a significant converse piezoelectric effect. The longitudinal piezoelectric d constants are estimated from the lattice parameters at $E = \pm 1$ MV/cm to be 9.8 and 10.1 pm/V for $\boldsymbol{E} \parallel \boldsymbol{x}$ and $\boldsymbol{E} \parallel \boldsymbol{z}$, respectively. For $\boldsymbol{E} \parallel \boldsymbol{x}+\boldsymbol{z}$ and $\boldsymbol{E} \parallel \boldsymbol{x}-\boldsymbol{z}$, both a and c show significant converse piezoelectric effects.

The ferroelectric crystal structures at $E = 0$ for $\boldsymbol{E} \parallel \boldsymbol{x}$ and $\boldsymbol{E} \parallel \boldsymbol{z}$ are crystallographically equivalent within numerical accuracy. Similarly, those for $\boldsymbol{E} \parallel \boldsymbol{x}+\boldsymbol{z}$ and $\boldsymbol{E} \parallel \boldsymbol{x}-\boldsymbol{z}$ are also equivalent. In our previous study [9], possible molecular arrangements and space groups were proposed for the two types of FE phases. The structures of two FE phases obtained in the present study are consistent with those results. Here, according to our previous study, these two FE phases are described as FE-α and FE-β. Imposing the crystallographic symmetries of Pm and Im proposed in our previous study [9], the crystal structures of the two FE phases were computationally refined. In Table II, the lattice parameters of the AFE, FE-α, and FE-β phases obtained using the rVV10 functional are listed together with their unit-cell volumes and space groups. The corresponding optimized atomic positions are listed in Table III. The differences in the lattice parameters are rather small among the three phases, including the AFE

TABLE II. Lattice parameters of the AFE, FE-α, and FE-β phases of SQA obtained using the rVV10 functional at $E = 0$. Their unit-cell volumes V and space groups (SG) are also listed.

	a (Å)	b (Å)	c (Å)	β (°)	V (Å^3)	SG
AFE	6.127	5.143	6.142	89.92	193.54	$P2_1/m$
FE-α	6.133	5.143	6.136	90.02	193.54	Pm
FE-β	6.134	5.147	6.132	90.00	193.60	Im

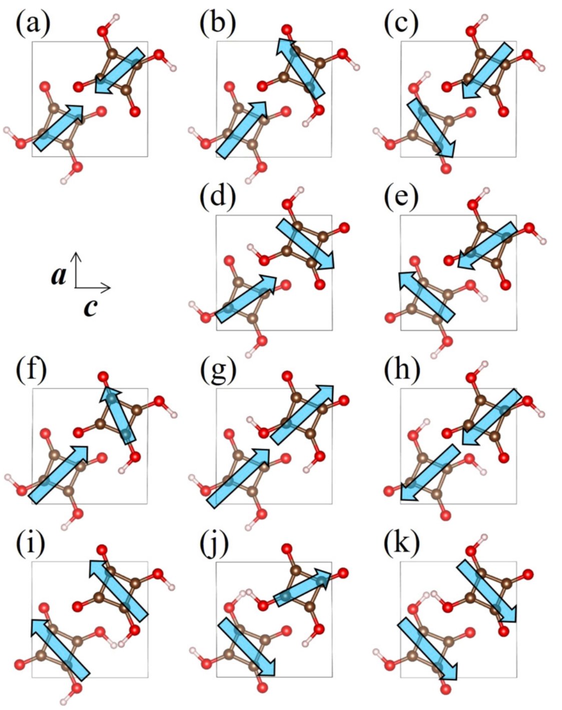

FIG. 3. Snapshots of molecular arrangements of SQA under electric field. The lower-left molecule is at $y = 0.25$, while the upper-right molecule is at $y = 0.75$. (a) Initial AFE phase; (b) $\boldsymbol{E} \parallel \boldsymbol{x}$, +7 MV/cm; (c) $\boldsymbol{E} \parallel \boldsymbol{x}$, −6 MV/cm; (d) $\boldsymbol{E} \parallel z$, +7 MV/cm; (e) $\boldsymbol{E} \parallel z$, −6 MV/cm; (f) $\boldsymbol{E} \parallel \boldsymbol{x} + z$, +9 MV/cm; (g) $\boldsymbol{E} \parallel \boldsymbol{x} + z$, +11 MV/cm; (h) $\boldsymbol{E} \parallel \boldsymbol{x} + z$, −8 MV/cm; (i) $\boldsymbol{E} \parallel \boldsymbol{x} - z$, +10 MV/cm; (j) $\boldsymbol{E} \parallel \boldsymbol{x} - z$, −8 MV/cm; (k) $\boldsymbol{E} \parallel \boldsymbol{x} - z$, +11 MV/cm. (b)–(k) correspond to the labels in Fig. 2. Arrows represent the sublattice polarization. Their lengths are proportional to the polarization amplitudes.

TABLE III. Optimized atomic positions of the AFE, FE-α, and FE-β phases of SQA obtained using the rVV10 functional at $E = 0$.

	x	y	z
AFE			
C	0.199558	0.25	0.096457
C	0.105735	0.25	0.308633
C	0.321135	0.25	0.410267
C	0.420573	0.25	0.187359
O	0.113463	0.25	−0.096249
O	−0.088980	0.25	0.391666
O	0.393967	0.25	0.599645
O	0.608582	0.25	0.109811
H	0.232348	0.25	−0.220646
H	−0.213189	0.25	0.272894
FE-α			
C	0.201598	0.0	0.098661
C	0.107892	0.0	0.310934
C	0.323414	0.0	0.412838
C	0.422484	0.0	0.189661
O	0.115385	0.0	−0.094393
O	−0.086772	0.0	0.393235
O	0.396718	0.0	0.602328
O	0.610175	0.0	0.111637
H	0.233774	0.0	−0.219126
H	−0.211064	0.0	0.274112
C	0.810740	0.5	0.896591
C	0.912496	0.5	0.681397
C	0.689522	0.5	0.582197
C	0.598189	0.5	0.802875
O	0.893706	0.5	1.091007
O	1.102116	0.5	0.607828
O	0.612426	0.5	0.394252
O	0.405028	0.5	0.888346
H	0.774301	0.5	1.214786
H	0.280655	0.5	0.768992
FE-β			
C	0.191526	0.0	0.078645
C	0.100370	0.0	0.299363
C	0.312828	0.0	0.393200
C	0.414633	0.0	0.177705
O	0.113806	0.0	−0.109279
O	−0.092817	0.0	0.384919
O	0.395092	0.0	0.587877
O	0.604030	0.0	0.103817
H	0.275273	0.0	0.711584
H	−0.217589	0.0	0.266147

phase, although the tetragonality slightly increases for the FE phases. The molecular shapes of the FE phases are almost the same as that of the AFE phase, except for their directions, as shown in Fig. 4.

We introduced a linear interpolation parameter λ to connect the AFE phase ($\lambda = 0$) and one of the FE phases ($\lambda = 1$). Intermediate structures were generated with 0.1 increments for λ. The lattice vectors at λ are obtained as $\boldsymbol{a}_\lambda = (1 - \lambda)\boldsymbol{a}_0 + \lambda \boldsymbol{a}_1$, $\boldsymbol{b}_\lambda = (1 - \lambda)\boldsymbol{b}_0 + \lambda \boldsymbol{b}_1$, $\boldsymbol{c}_\lambda = (1 - \lambda)\boldsymbol{c}_0 + \lambda \boldsymbol{c}_1$, where the suffixes "0" and "1" represent $\lambda = 0$ and 1, respectively. Similarly, the fractional coordinates of the nth atom are obtained as $x_{n\lambda} = (1 - \lambda)x_{n0} + \lambda x_{n1}$, $y_{n\lambda} = (1 - \lambda)y_{n0} + \lambda y_{n1}$, $z_{n\lambda} = (1 - \lambda)z_{n0} + \lambda z_{n1}$. Only a few hydrogen atoms show significant relative displacements with reference to the molecular center, as shown in Fig. 4.

Figure 5 represents the variation in the total energy and the polarization vector components as a function of λ. The polarization component along $\boldsymbol{b}$ is zero because of the mirror symmetry. For FE-α, only one hydrogen atom per unit cell switches its position along the hydrogen bond. The corresponding energy barrier (energy variation from $\lambda = 0$ to 0.5) is 79.8 meV, which is close to the value of 87 meV obtained by Wikfeldt and Michaelides [34] using the vdW-DF2 functional [35]. For FE-β, the energy barrier is 162.5 meV, which is twice as high as that for FE-α, reflecting the fact that two hydrogen atoms switch their positions in FE-β. The total energy values per unit cell of FE-α and FE-β are 2.5 and 4.9 meV higher than that of AFE, respectively. Again, the electronic interaction between the sublattices seems to be not strong. These values might be underestimated, as the AFE phase is always stable at room temperature. The total polarization amplitude is 14.5 μC/cm^2 for FE-α and 20.6 μC/cm^2 for FE-β. The former value is in reasonable agreement with the experimental value of 10.5 μC/cm^2 [9] for a system considered as the FE-α phase. Although the FE-β phase has not yet been experimentally confirmed, the value of 20.6 μC/cm^2 is relatively high among those of the existing organic ferroelectrics [36–42]. The present

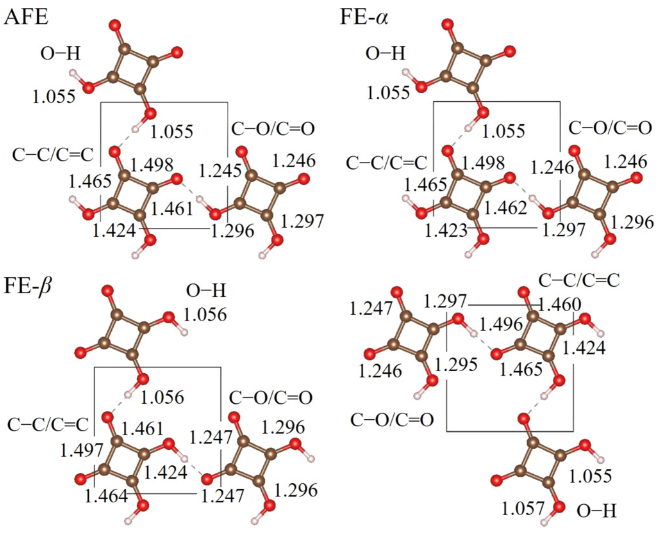

FIG. 4. Bond lengths (Å) in the AFE (upper left), FE-α (right), and FE-β (lower left) phases of SQA obtained using the rVV10 functional at $E = 0$.

values are consistent with the previous estimates from the sublattice polarization of the AFE phase [9,43].

We evaluated the polarization contribution on the basis of the proton motion using the point charge model, where $+|e|$ charge is the charge observed at each proton and $-2|e|$ charge is the charge observed at each C_4O_4 molecular core center (e: electron charge). The resultant polarization vectors are (2.5, 0.0, 2.4) and (4.9, 0.0, -0.1) $\mu C/cm^2$ for the FE-α and FE-β phases, respectively. Each of their amplitudes is less than $1/4$ of the corresponding total polarization amplitude. As already mentioned in our previous study [9], the rearrangement of the π electrons due to proton transfer plays a predominant role in the polarization variation.

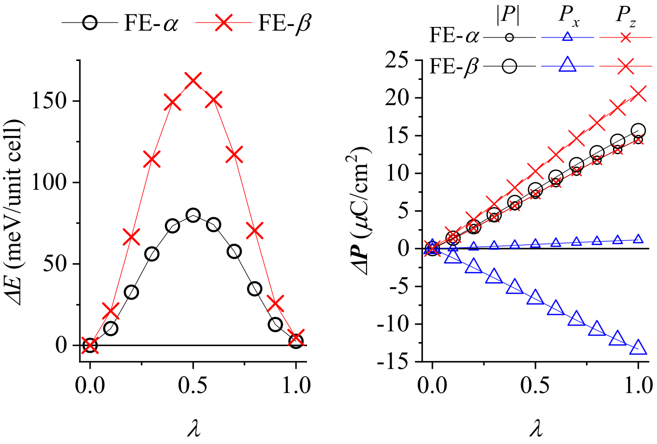

FIG. 5. Variation in total energy (left) and polarization vector components (right) of SQA as a function of λ. For the AFE phase, $\lambda = 0$, while for the FE-α or FE-β phase, $\lambda = 1$.

IV. CONCLUSIONS

We have successfully reproduced the AFE-to-FE transition in SQA via computational simulations, where the optimized crystal structure and the corresponding polarization vector are calculated with varying the electric field $\boldsymbol{E}$. Depending on the $\boldsymbol{E}$ direction, the polarization vector can be aligned in eight different directions. Two metastable ferroelectric phases have been identified along with their crystal structures. One of the phases is yet to be experimentally confirmed. Their spontaneous polarization values and converse piezoelectric coefficients have been evaluated. The spontaneous polarization values are relatively high among those of the existing organic ferroelectrics. We hope that the present study will pave the path for further research on organic antiferroelectrics.

ACKNOWLEDGMENTS

This work was partially supported by JSPS KAKENHI Grant No. JP16H02301 and by Priority Issue (creation of new functional devices and high-performance materials to support next-generation industries) to be tackled by using Post 'K' Computer, Ministry of Education, Culture, Sports, Science and Technology, Japan. Some calculations have been performed using the facilities of the Supercomputer Center, the Institute for Solid State Physics, the University of Tokyo.

---

[1] C. Kittel, Phys. Rev. **82**, 729 (1951).
[2] E. Sawaguchi, H. Maniwa, and S. Hoshino, Phys. Rev. **83**, 1078 (1951).
[3] G. Shirane, E. Sawaguchi, and Y. Takagi, Phys. Rev. **84**, 476 (1951).
[4] S. Horiuchi, F. Kagawa, K. Hatahara, K. Kobayashi, R. Kumai, Y. Murakami, and Y. Tokura, Nat. Commun. **3**, 1308 (2012).
[5] K. M. Rabe, in *Functional Metal Oxides: New Science and Novel Applications*, edited by S. B. Ogale, T. V. Venkatesan, and M. G. Blamire (Wiley-VCH, Weinheim, 2013), Vol. 7, p. 221.
[6] X. Hao, J. Zhai, L. B. Kong, and Z. Xu, Prog. Mater. Sci. **63**, 1 (2014).
[7] M. H. Park, Y. H. Lee, H. J. Kim, Y. J. Kim, T. Moon, K. D. Kim, J. Müller, A. Kersch, U. Schroeder, T. Mikolajick, and C. S. Hwang, Adv. Mater. **27**, 1811 (2015).
[8] J. Feder, in *Oxocarbons*, edited by R. West (Academic, New York, 1980), Vol. 8, p. 141.
[9] S. Horiuchi, R. Kumai, and S. Ishibashi, Chem. Sci. **9**, 425 (2018).
[10] D. Semmingsen, F. J. Hollander, and T. F. Koetzle, J. Chem. Phys. **66**, 4405 (1977).
[11] D. M. Ceperley and B. J. Alder, Phys. Rev. Lett. **45**, 566 (1980).
[12] J. P. Perdew and A. Zunger, Phys. Rev. B **23**, 5048 (1981).
[13] J. P. Perdew, K. Burke, and M. Ernzerhof, Phys. Rev. Lett. **77**, 3865 (1996).
[14] K. Berland and P. Hyldgaard, Phys. Rev. B **89**, 035412 (2014).
[15] O. A. Vydrov and T. Van Voorhis, J. Chem. Phys. **133**, 244103 (2010).

[16] R. Sabatini, T. Gorni, and S. de Gironcoli, Phys. Rev. B **87**, 041108(R) (2013).

[17] M. Dion, H. Rydberg, E. Schroder, D. C. Langreth, and B. I. Lundqvist, Phys. Rev. Lett. **92**, 246401 (2004).

[18] S. Ishibashi, T. Tamura, S. Tanaka, M. Kohyama, and K. Terakura, Phys. Rev. B **76**, 153310 (2007).

[19] P. E. Blöchl, Phys. Rev. B **50**, 17953 (1994).

[20] J. Wu and F. Gygi, J. Chem. Phys. **136**, 224107 (2012).

[21] M. Obata, M. Nakamura, I. Hamada, and T. Oda, J. Phys. Soc. Jpn. **84**, 024715 (2015).

[22] G. Román-Pérez and J. M. Soler, Phys. Rev. Lett. **103**, 096102 (2009).

[23] W. H. Press, S. A. Teukolsky, W. T. Vetterling, and B. P. Flannery, *Numerical Recipes in Fortran 77*, 2nd ed. (Cambridge University Press, New York, 1992).

[24] E. Bitzek, P. Koskinen, F. Gähler, M. Moseler, and P. Gumbsch, Phys. Rev. Lett. **97**, 170201 (2006).

[25] G. P. Francis and M. C. Payne, J. Phys.: Condens. Matter **2**, 4395 (1990).

[26] I. Souza, J. Íñiguez, and D. Vanderbilt, Phys. Rev. Lett. **89**, 117602 (2002).

[27] R. D. King-Smith and D. Vanderbilt, Phys. Rev. B **47**, 1651 (1993).

[28] R. Resta, Rev. Mod. Phys. **66**, 899 (1994).

[29] S. Ishibashi and K. Terakura, Physica B (Amsterdam) **405**, S338 (2010).

[30] S. Ishibashi, K. Terakura, and S. Horiuchi, J. Phys. Soc. Jpn. **79**, 043703 (2010).

[31] D. Semmingsen, Z. Tun, R. J. Nelmes, R. K. McMullan, and T. F. Koetzle, Z. Kristallogr. **210**, 934 (1995).

[32] D. Di Sante, A. Stroppa, and S. Picozzi, Phys. Chem. Chem. Phys. **14**, 14673 (2012).

[33] H. Moriwake, A. K. T. Ogawa, C. A. J. Fisher, A. Kuwabara, and D. Fu, J. Appl. Phys. **119**, 064102 (2016).

[34] K. T. Wikfeldt and A. Michaelides, J. Chem. Phys. **140**, 041103 (2014).

[35] K. Lee, É. D. Murray, L. Kong, B. I. Lundqvist, and D. C. Langreth, Phys. Rev. B **82**, 081101 (2010).

[36] S. Horiuchi, Y. Tokunaga, G. Giovannetti, S. Picozzi, H. Itoh, R. Shimano, R. Kumai, and Y. Tokura, Nature (London) **463**, 789 (2010).

[37] K. Kobayashi, S. Horiuchi, R. Kumai, F. Kagawa, Y. Murakami, and Y. Tokura, Phys. Rev. Lett. **108**, 237601 (2012).

[38] S. Horiuchi, K. Kobayashi, R. Kumai, and S. Ishibashi, Chem. Lett. **43**, 26 (2014).

[39] F. Kagawa, S. Horiuchi, N. Minami, S. Ishibashi, K. Kobayashi, R. Kumai, Y. Murakami, and Y. Tokura, Nano Lett. **14**, 239 (2014).

[40] K. Kobayashi, S. Horiuchi, S. Ishibashi, F. Kagawa, Y. Murakami, and R. Kumai, Chem. Eur. J. **20**, 17515 (2014).

[41] S. Horiuchi, Y. Noda, T. Hasegawa, F. Kagawa, and S. Ishibashi, Chem. Mater. **27**, 6193 (2015).

[42] S. Horiuchi, K. Kobayashi, R. Kumai, and S. Ishibashi, Nat. Commun. **8**, 14426 (2017).

[43] F. Ishii, N. Nagaosa, Y. Tokura, and K. Terakura, Phys. Rev. B **73**, 212105 (2006).